

Bubble velocimetry using the conventional and CNN-based optical flow algorithms

Hyungmin Park (✉ hminpark@snu.ac.kr)

Seoul National University

Daehyun Choi

Seoul National University

Hyunseok Kim

Seoul National University

Article

Keywords: bubble velocimetry, optical flow, image processing, deep learning, convolutional neural network (CNN), bubbly flow, multiphase flow

Posted Date: April 7th, 2022

DOI: <https://doi.org/10.21203/rs.3.rs-1503370/v1>

License: © ⓘ This work is licensed under a Creative Commons Attribution 4.0 International License.

[Read Full License](#)

Bubble velocimetry using the conventional and CNN-based optical flow algorithms

Daehyun Choi^{1,a)}, Hyunseok Kim^{1,a),b)} and Hyungmin Park^{1,2,c)}

¹Department of Mechanical Engineering, Seoul National University, Seoul 08826, Korea

²Institute of Advanced Machines and Design, Seoul National University, Seoul 08826, Korea

Abstract

In the present study, we introduce new bubble velocimetry methods based on the optical flow, which were validated (compared) with the conventional particle tracking velocimetry (PTV) for various gas-liquid two-phase flows. For the optical flow algorithms, the convolutional neural network (CNN)-based models as well as the original schemes like the Lucas-Kanade and Farnebäck methods are considered. In particular, the CNN-based method was re-trained (fine-tuned) using the synthetic bubble images produced by varying the density, diameter, and velocity distribution. While all models accurately measured the unsteady velocities of a single bubble rising with a lateral oscillation, the pre-trained CNN-based method showed the discrepancy in the averaged velocities in both directions for the dilute bubble plume. In terms of the fluctuating velocity components, the fine-tuned CNN-based model produced the closest results to that from PTV, while the conventional optical flow methods under- or over-estimated them owing to the intensity assumption. When the void fraction increases much higher (e.g., over 10%) in the bubble plume, the PTV failed to evaluate the bubble velocities because of the overlapped bubble images and significant bubble deformation, which is clearly overcome by the optical flow bubble velocimetry. This is quite encouraging in experimentally investigating the gas-liquid two-phase flows of a high void fraction. Furthermore, the fine-tuned CNN-based model captures the individual motion of overlapped bubbles most faithfully while saving the computing time, compared to the Farnebäck method.

Keywords: bubble velocimetry, optical flow, image processing, deep learning, convolutional neural network (CNN), bubbly flow, multiphase flow

^{a)}Equally contributed to this work.

^{b)}Present address: Environment & Safety Research Center, Samsung Electronics, Hwaseong, 18448, Korea

^{c)}Author to whom correspondence should be addressed: hminpark@snu.ac.kr

INTRODUCTION

Interfacial momentum exchange between continuous and dispersed phases is very important in understanding the physics of multiphase flows, in particular, for the gas-liquid two-phase flows, where the gas-liquid interface deforms in a complex manner and the mutual interaction between the phases are correlated^[1-10]. Since the interfacial forces (e.g., drag, lift, added mass and basset history forces) acting on the rising bubbles in a liquid flow^[11-13] and the bubble-induced agitation (pseudo-turbulence) to the liquid flow^[5, 8, 14-19] are strongly determined by the bubble velocity (motion) relative to the liquid-phase, it is critical to have the detailed information of bubble velocities. To cope with this, the image-based velocimetry techniques (e.g., two-phase particle image velocimetry and shadowgraphy) to obtain the gas-phase statistics have been proposed widely. Recently, Kim & Park^[7] developed a universal and automated bubble detection method based on the Mask R-CNN deep-learning algorithm, which was shown to be very successful in extracting and tracking the bubble shapes in the images obtained from different flow geometries and optical configurations.

In addition to the bubble shape (i.e., interface morphology), on the other hand, it is also important to measure the bubble velocity, as it is relevant to the interfacial forces. Most of the previous studies have used the particle tracking velocimetry (PTV) algorithm to evaluate the bubble velocity, based on the centroid of each bubble on the images obtained optically. The

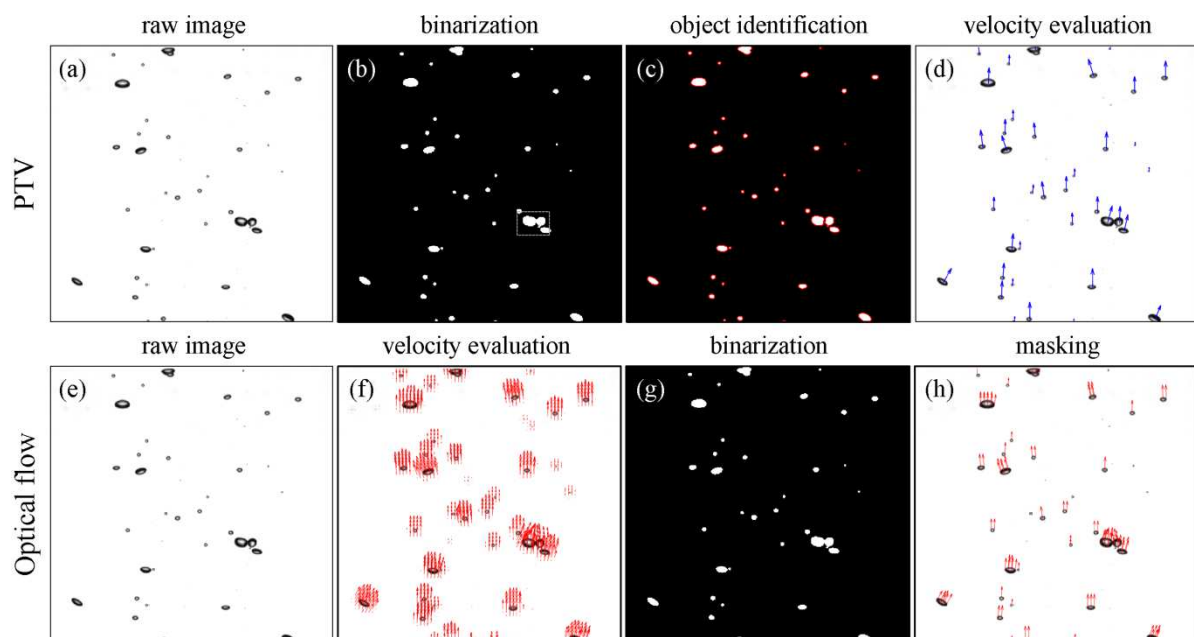


Fig. 1. Typical procedure of evaluating the bubble velocities from the shadowgraph image of the bubbly flow: (a-d) conventional PTV and (e-h) optical flow (Farneback) method.

typical process of PTV applied for the shadow image (taken for the bubbly flow) consists of the binarization, identification, and evaluation, as shown in Figs. 1(a)-(d). First, the bubble is individually recognized and tagged as an identical object in the images that were successively obtained (Figs. 1(b) and (c)). Next, the distance traveled by each bubble centroid is divided by the time interval between consecutive images, which results in the bubble velocities (Fig. 1(d)). The bubble velocity from the PTV is obtained from a clear physical background and thus guarantees the high accuracy, if specific conditions are satisfied such as the low void fraction ($< 2.5\%$) and mild shape deformation, enabling the exact matching of each bubble^[4, 5, 8]. In other words, this conventional method has limitations to be applied to wider circumstances: (i) the computing costs to evaluate the whole velocity fields get increasing significantly with increasing the number of images, (ii) it is difficult to reflect the effect of local deformation of the bubble (only a single velocity vector is obtained for one bubble), and most importantly (iii) it cannot be used for the bubbly flows with a higher void fraction, i.e., for highly overlapped bubbles. The computing cost of the PTV is mainly consumed during the process of identifying individual bubbles. As noted in Table 1, for processing one pair of images, the step of individual object (bubble) identification costs 0.812 sec, which is 95% of the entire procedure. On the other hand, the PTV only tracks the bubble centroid to obtain the velocity, and thus, the bubble deformation is ignored, which is known to affect the interaction between the bubble and the surrounding flow^[8, 20-24]. It would be important as well as interesting to investigate the velocity of local bubble surface, which is different from that of the centroid^[25-27].

Table 1. Comparison of the computing costs of each method for evaluating the bubble velocities in a single pair of dilute plume images (size of 400×608 pixels; see Fig. 7). The PTV and the conventional optical flows are operated by CPU (Intel® Core™ i7-5960X CPU @3.00GHz), whereas the CNN-based optical flow uses GPU (GeForce RTX2080 12GB). It is noted that only the PTV method requires the step of object (bubble) identification.

Cost	PTV	Lucas-Kanade method	Farneback method	CNN-based model
Object identification	0.812 sec	-	-	-
Vector evaluation	0.041 sec	0.025 sec	0.155 sec	0.033 sec
Total	0.853 sec	0.025 sec	0.155 sec	0.033 sec

The most critical drawback of the PTV would be the difficulty in calculating the bubble velocity of highly overlapped and deformed bubbles (e.g., see Fig. 2(c) for the dense bubble plume). Here, the overlap denotes the actual contact of bubbles (or their projections) on the two-dimensional image (see the dashed box in Fig. 1(b)). Previous studies tried to deal with this issue by dividing the overlapped bubbles using the watershed transform^[28] or ignoring the overlapped bubbles altogether^[8]. Watershed transform is a method of recognizing and classifying bubbles based on the bright local maxima that appear at the bubble center region^[5]. However, if multiple (more than three) bubbles are simultaneously overlapped or there are multiple maxima in one bubble (typically this happens when the bubble size becomes larger), the bubbles are not clearly distinguished based on the maxima^[7]. For the PTV, the identification of the individual bubble is a prerequisite for the velocity evaluation and it can significantly deteriorate the reliability of the calculated velocity vectors. Therefore, the PTV has been mostly used for the case of the relatively small bubble (less than 4 mm of the diameter) experiencing the milder shape deformation, with a lower volume void fraction (Figs. 2(a) and (b)). However, the bubbly flows that are easily found in nature and industry have a higher volume void fraction, which requires a new method that can accurately and systematically measure the velocity field from a number of deformable and overlapped bubbles.

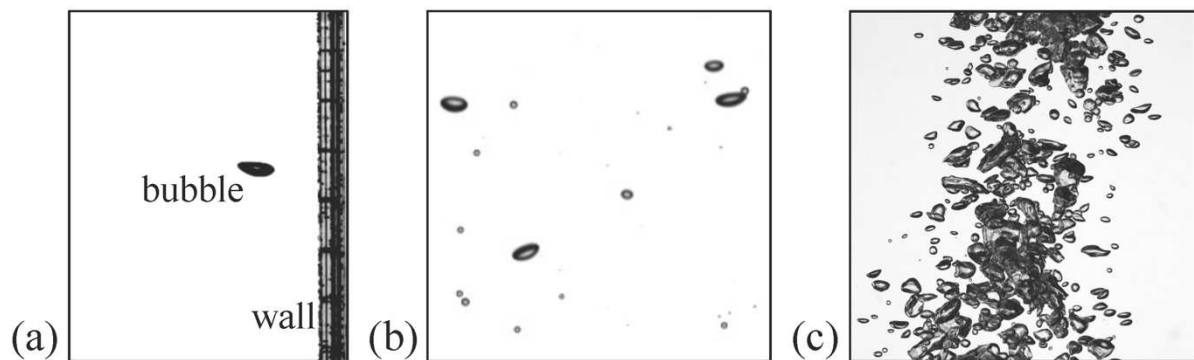


Fig. 2. Bubbly flows from different environments: (a) single bubble rising near the vertical wall, (b) dilute bubble plume (void fraction of 1.13%), (c) dense bubble plume (void fraction of 58%).

As a promising solution to this problem, we propose the optical flow algorithm as a bubble velocimetry method. The optical flow is a technique to evaluate the velocity field based on the change of the light intensity (not dependent on the object) in the consecutive images with the assumptions that (i) the brightness of each material point has a constant value in the consecutive images, i.e., brightness constancy, (ii) the displacement is sufficiently small, and (iii) the flow

field is smoothly evolving^[29-31]. Here, we brief the general procedure to obtain the vector field using the optical flow algorithm, and the details can be found in elsewhere^[32, 33]. If the gray value $I(x, y, t)$ on the position of (x, y) at any time t moves to $(x+\delta x, y+\delta y)$ after the time interval of δt , the brightness constancy condition can be expressed as the Eq. (1).

$$I(x + \delta x, y + \delta y, t + \delta t) = I(x, y, t) \quad (1)$$

Applying the first-order Taylor series expansion to the left-hand side of the Eq. (1), we have

$$I(x + \delta x, y + \delta y, t + \delta t) \cong I(x, y, t) + \frac{\partial I}{\partial x} \delta x + \frac{\partial I}{\partial y} \delta y + \frac{\partial I}{\partial t} \delta t. \quad (2)$$

When the Eq. (2) is replaced into the Eq. (1), it is further simplified to $I_x u + I_y v = -I_t$, where $I_x = \partial I / \partial x$, $I_y = \partial I / \partial y$, $I_t = \partial I / \partial t$, and (u, v) denotes the velocity field on the (x, y) plane. In order to solve this equation, the information about two or more points (x, y) , i.e., the gradients, is required, and it is applied on the window basis, instead of a single point. Let's consider a window of $N \times M$ size (i.e., it consists of points of $\mathbf{q}_1, \mathbf{q}_2, \dots, \mathbf{q}_{N \times M}$). If each point on the window has the same velocity (u, v) , then the Eq. (3) can be established.

$$\begin{bmatrix} I_x(\mathbf{q}_1) & I_y(\mathbf{q}_1) \\ I_x(\mathbf{q}_2) & I_y(\mathbf{q}_2) \\ \vdots & \vdots \\ I_x(\mathbf{q}_{N \times M}) & I_y(\mathbf{q}_{N \times M}) \end{bmatrix} \begin{bmatrix} u & v \end{bmatrix} = - \begin{bmatrix} I_t(\mathbf{q}_1) \\ I_t(\mathbf{q}_2) \\ \vdots \\ I_t(\mathbf{q}_{N \times M}) \end{bmatrix} \quad (3)$$

Here, we have $N \times M$ equations for two unknowns, and thus the single solution (u, v) can be determined through the least-square method. As noted, the key element of the Lucas-Kanade algorithm is that it approximates the image intensity using the first-order Taylor series expansion^[32]. On the other hand, Farneback^[33] modified the algorithm such that it can measure the displacement of each point in the consecutive images by assuming that the image intensity is a quadratic function with respect to the position (x, y) . This method costs quite more than the Lucas-Kanade model (see Table 1), but it was shown to provide more accurate and detailed velocity fields.

Recently, the convolutional neural network (CNN)-based optical flow has been suggested to elevate not only the spatial resolution but also the accuracy, compared with the conventional optical flow^[34, 35]. For example, the series of convolutional networks (FlowNet) with converging and diverging structures have been proven to produce more accurate velocity fields of the single-phase flow with a higher resolution than the conventional optical flow^[34]. On the

other hand, Sun *et al.*^[35] proposed the system of the convolutional network (PWC-Net), analogous to the coarse-to-fine adaptive approach of the conventional optical flow (which obtains the velocity fields of the higher spatial-resolution using the pre-calculated velocity field from the under-sampled image), and used it to obtain the velocity field of daily objects (e.g., SINTEL animation, the KITTI dataset, and flyingchairs dataset). It was shown that it is cost-effective and more accurate than the FlowNet and conventional optical flow models. In the present study, we selected this PWC-Net to evaluate the bubble velocity and also re-trained it with the synthetic bubble images.

The network architecture of PWC-Net comprises two fixed-parameter layers consisting of the warping and cost volume, and three trainable-parameter layers consisting of the feature extraction, velocity field estimator, and context network. First, the two consecutive raw images are inserted to the feature extracting layer that is the converging convolutional networks with n -levels, and each level of the layer produces a different resolution of 'features' (i.e., the product of each convolutional filter). At the lowest-resolution feature, the cost-volume layer and the velocity field estimator evaluate the draft of the velocity field, which is finally converted to the velocity field data through the context layer. This coarser version of velocity data is subsequently updated to the next-high level of layer and is used to deform one of two features to achieve the better prediction of the velocity field. Likewise, the two features from the consecutive images at the next level of the layer are converted to the velocity vector with a higher resolution. In the present study, the number of flow prediction and pyramid levels is set to six and two, respectively. The weights are pre-trained with the KITTI and 3D-FlyingChair datasheet (for the detailed procedure, please refer to Sun *et al.*^[35]), since the application of the CNN-based optical flow has been mainly focused on the identification of large objects such as humans in the avenue, vehicles, and daily objects. However, it has been reported that the CNN-based model can perform like the particle image velocimetry (PIV) and significantly enhances the spatial resolution by fine-tuning (i.e., further training with the dataset of interest)^[36, 37], compared to the conventional PIV^[38, 39]. As an advantage of the optical flow method, they pointed out that it can account for the non-linear deformation of the flow, and claimed that the CNN-based optical flow is capable of measuring the velocity field based on the particle distribution. We are interested in investigating how this CNN-based model would perform in measuring the velocity of highly deformable bubbles, more complex than the translational particle movement.

Therefore, in the present study, we consider the Lucas-Kanade and Farneback models as representatives of the conventional optical flow algorithm, two CNN-based models (PWC-Net) that are pre-trained and fine-tuned, and their applications to some bubbly flows (the rise of a single bubble, dilute bubble plume, and dense bubble plume; Fig. 2) are compared with the results from the PTV. The synthetic bubble images were separately created for the fine-tuning (training), which has been proven to significantly enhance the accuracy of the model^[7]. For the validation, the experiments were performed to generate the bubble shadow images in different environments using a high-speed camera. Each optical flow algorithm, together with the PTV, is assessed in terms of the accuracy and time cost. We hope the present results will be widely utilized in relieving the difficulties in the dynamic analysis of the optical images having multiple objects, and accelerating the experimental studies of bubbly flows in complex geometries.

CONFIGURATION of the OPTICAL FLOW MODEL

Conventional optical flow model

For the conventional optical flow, two consecutive bubble images are segmented into a small window, in which the displacement vectors are generated. Therefore, the density of the window determined by its size and overlap ratio is related to the spatial resolution of the velocity field, and thus, they should be carefully selected. To examine the dependency on the window size, the vertical velocity of the bubbles in a dilute plume, shown in Fig. 2(b), is measured with three different window sizes of 7×7 , 21×21 , and 31×31 pixels using the Lukas-Kanade method. Fig. 3(a) shows that the vertical velocity tends to be underestimated as the window size becomes smaller, compared to the result of the PTV. This indicates that there exists a certain threshold of window size above which the optical flow would perform well, which is found to depend on the bubble size. The probability density function of the measured bubble size distribution is plotted in Fig. 3(b), together with the relative position of three window sizes. As shown, the window size of 7×7 pixels is smaller than the averaged bubble size of 3.4 mm, but two larger windows are comparable (or larger) than that. Thus, it is learned that the window size should be at least as large as the average size of the bubbles that are to be measured. Based on this finding, we tested various sizes of windows for Lukas-Kanade and Farneback methods, by applying them to the flows with lower number density of bubbles (Figs. 2(a) and (b)). For

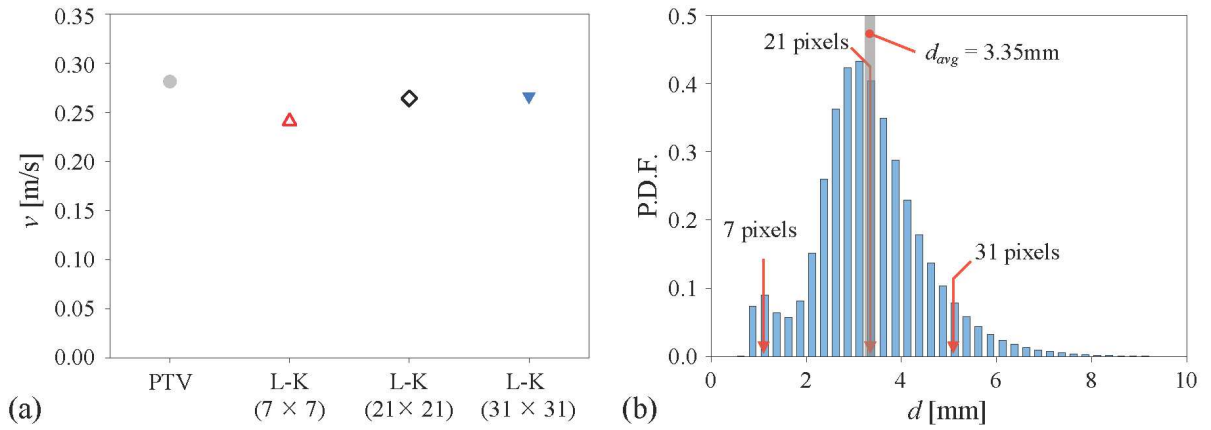


Fig. 3. Effect of window size on the optical flow measurement: (a) Horizontal profile of averaged vertical velocity (●, PTV; △, Lukas-Kanade method with the window size of 7×7 ; ◇, 21×21 ; ▼, 31×31 pixels); (b) probability density function of measured bubble size (solid lines denote the tested window sizes). Here, the measurements were done for the dilute bubble plume (Fig. 2(b)) with the mean bubble diameter of 3.4 mm and void fraction of 1.13%.

the Lukas-Kanade method, as we have discussed, the accuracy of the measured bubble velocity was enhanced as the window size is slightly larger than the averaged bubble diameter, while the Farneback method was less sensitive to the window size. As a result, the window size for the Lukas-Kanade method was set to 21×21 pixels for the single bubble (Fig. 2(a)) and 31×31 pixels for bubble plumes (Figs. 2(b) and (c)). It was fixed as 7×7 pixels for the Farneback method. The overlap ratio of 50% and 0% was applied for the Lukas-Kanade and Farneback methods, respectively. Since the conventional optical flow evaluates the velocity vector by the window, velocity fields cover a slightly larger area than the bubbles (Fig. 1(f)), and a simple masking process is applied afterward to remove the velocity vectors located outside of the bubble. Here, the binarization process is the same as that of the PTV (Fig. 1(b)). Since the optical flow technique does not require the object identification (Fig. 1(c)), it costs much less time (see Table 1).

CNN-based optical flow model

In contrast to the conventional optical flow, the PWC-Net^[35] is free from the window size because the whole velocity vector field is obtained at once. Instead, the hyperparameter (e.g., number of layers, epochs, and batch size) for the networks may affect the estimation. The model is trained following the learning schedule, as introduced in Sun *et al.*^[35], which reduces the

learning rate (initially starting from 10^{-5}) by half at 160k, 240k, 320k, and 400k epochs, with the batch size of 4. As the trainable layers, the feature extraction, the context section, and the velocity field estimator consist of 6, 7, and 2 layers, respectively. To examine the effect of such parameters, we used the weights of the model both pre-trained by the previous work^[35] and fine-tuned with the synthetic bubble images and their velocity fields, generated by the in-house Python code. Fig. 4 shows the representative synthetic bubble images and the corresponding velocity contours. The shape of the synthetic bubble was designated to be a randomly deformed ellipse with the size of 25-250 pixels, including the local maxima (i.e., the bright area inside the bubble shadow image caused by the refraction of background light) at its center region (Figs. 4(a) and (d)). The number of bubbles is 50-200 in one image pair. The synthetic bubbles are displaced with the random displacement of 10-50 pixels per frame (Figs. 4(b) and (e)), by which the corresponding velocity fields can be obtained as shown in Fig. 4(c) and (f), respectively. To enhance the robustness to the noises that can exist in bubble images, the intensity of the background was varied in the range of 0.1-0.9 (0 and 1 stands for the darkest and brightest intensity, respectively) at each pair, and the transparent rectangular bar and particles with the size of 1-5 pixels are also positioned at random. Finally, 100,000 pairs of

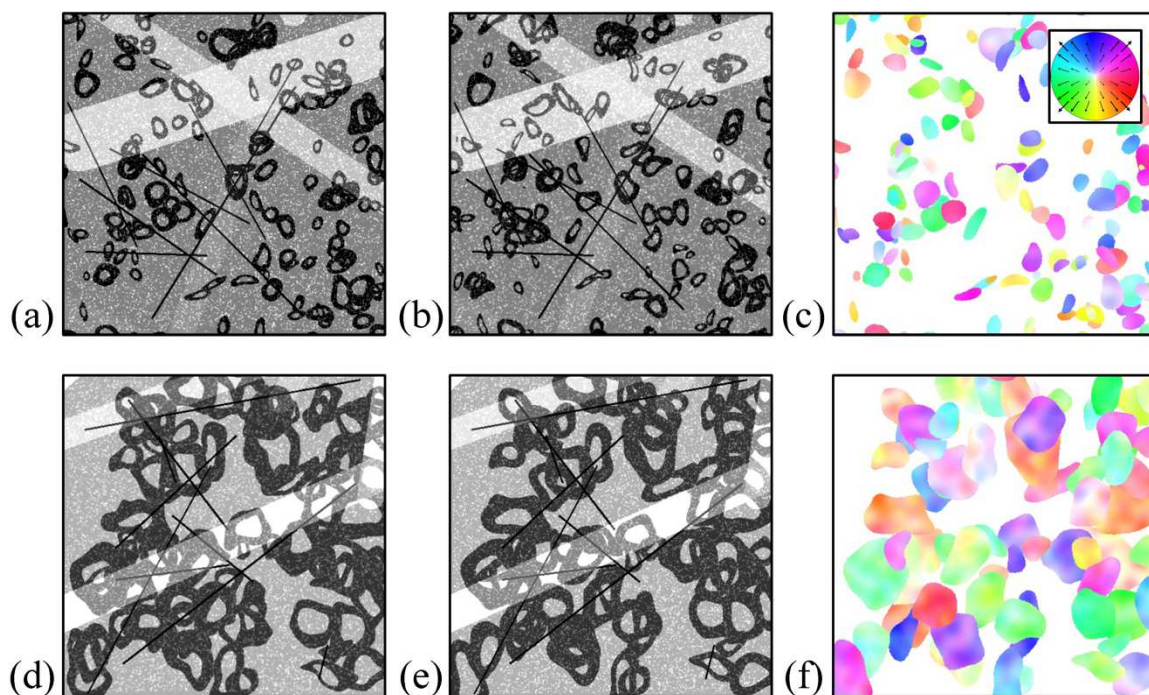


Fig. 4. Pair of synthetic bubble images used for the fine-tuning dataset for the PWC-Net: (a, b) small bubbles (bubble size = 10 - 60 pixels); (d, e) large bubbles (bubble size = 40 - 130 pixels); (c, f) contour of bubble velocity corresponding to each pair. The inset figure in (c) shows the direction and magnitude of velocity, expressed in terms of the hue and saturation, respectively.

bubble images (and the velocity fields) were generated and used to fine-tune the weights of the networks. The optimizer is selected as the ADAM scheme. The specification of the workstation that we have used is a single NVIDIA RX 2080 Ti GPU, and the calculation procedure (velocity field is calculated from the network and masked based on the binarization) is similar to the conventional optical flows (Figs. 1(e)-(h)).

Comparison on the computational costs

The computational cost of each method is summarized in Table 1. Processing a single pair of images taken for the dilute plume (Fig. 2(b)) to obtain the bubble velocities took 0.85, 0.025, 0.16, and 0.033 sec for the PTV, Lukas-Kanade, Farneback, and CNN-based models, respectively. Here, the CNN-based model used the GPU (GeForce RTX2080 12GB) to calculate the vector field, whereas the other models used the CPU (Intel® Core™ i7-5960X CPU @3.00GHz). As explained, the PTV method requires the longest computational time, mainly originating from the bubble identification step. The Lukas-Kanade takes the smaller cost than the CNN-based model, thanks to its simple assumption on treating the image intensity. On the other hand, the cost of the Farneback method is much greater than the CNN-based model, due to the higher-order modeling. Together with this comparison, we will discuss the reliability (accuracy) of the measured bubble velocities in the below.

RESULTS and DISCUSSION

Evaluation of the optical flows as a bubble velocimetry

To compare the characteristics and performance of optical flow methods, each algorithm is applied to the bubbly flows of different conditions (Fig. 2). First, we will start with the simplest case of a single bubble rising near the vertical wall, with the periodic lateral oscillation (Fig. 2(a)), and next discuss the results with the rise of several bubbles (without a significant overlap) in a dilute plume (Fig. 2(b)). Finally, the case of large population of deformable bubbles (with a significant overlap) in a dense plume (Fig. 2(c)) will be tested.

Single bubble rising near the vertical wall

Fig. 5 compares the velocity vector of a single bubble near the vertical wall, obtained by each method. As noted, one velocity vector at the bubble centroid is captured from the PTV (Fig. 5(b)), while the optical flow algorithms provide multiple velocity vectors, i.e., including the information about the local movement (deformation), assisted by the intensity-based measurement mechanism (Figs. 5(c)-(f)). Regardless of the method used, it is observed that the velocity vectors are oriented along the same direction, while the detailed pattern of velocity distribution differs. With the Lucas-Kanade method, velocity vectors located at the periphery of the bubble, characterized by the large curvature, tend to tilt toward the averaged travel direction of the bubble (Fig. 5(c)), whereas they are directed outward with the Farnebäck and two CNN-based models (Figs. 5(d)-(f)). Observing the interfacial deformation of the bubble, the peripheral regions expand while the middle area of the bubble tends to bulge up (see the arrows in Fig. 5(a)), which is more reliably detected by the Farnebäck and CNN-based models than the Lucas-Kanade method.

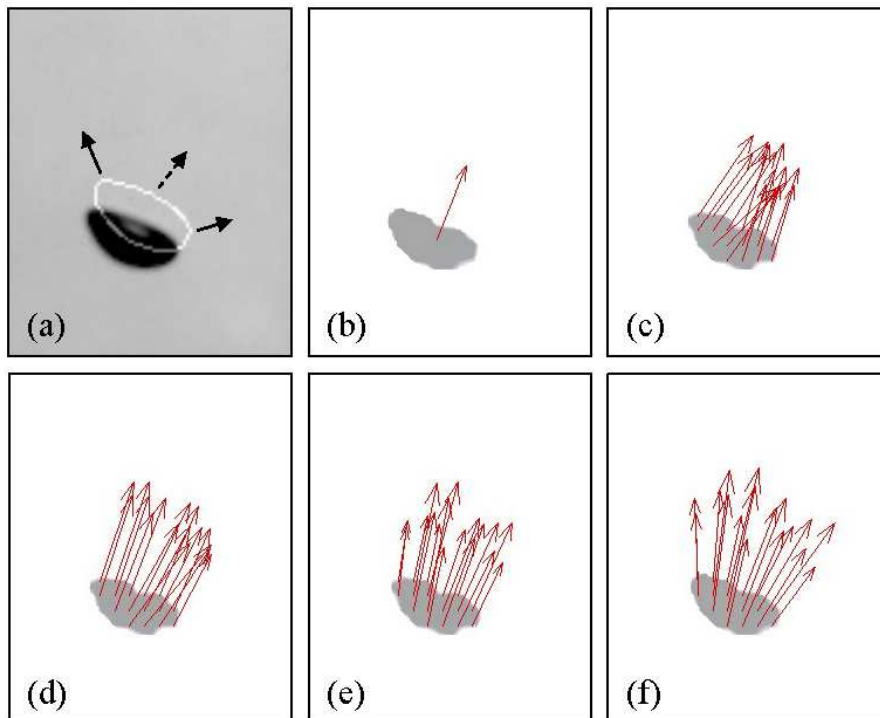


Fig. 5. Evaluation of the velocity of a single bubble (size of 3.5 mm): (a) the instant raw image with the bubble morphology at the next time step (after 30 msec) overlapped with a solid line; (b) result of the PTV; (c) Lukas-Kanade method; (d) Farnebäck method; (e) pre-trained CNN-based model; (f) fine-tuned CNN-based model. The gray shadow in (b-f) corresponds to the bubble shadow in (a).

For further quantitative evaluation, the time history of horizontal and vertical velocity components (for the same bubble in Fig. 5) is plotted in Fig. 6. For the data obtained from the optical flow methods, the averaged value of the velocities inside the bubble is used as a representative velocity. As shown, it is found that optical flow methods can accurately measure the temporally varying velocities of a moving bubble, being compared with the conventional PTV data. It is interesting to see that the pre-trained PWC-Net^[35] can reasonably provide the bubble velocity data suggesting its versatility, although it was not trained (or optimized) for the bubble velocimetry. However, the pre-trained CNN model predicts the slightly lower horizontal velocity at $t = 0.08$ and 0.22 sec, which correspond to the instances when the bubble collides with the wall, and it is thought that the pre-trained model is limited in distinguishing the wall and bubble shadow (Fig. 6(b)). On the other hand, the fine-tuned model (re-trained with the synthetic bubble images) seems to overcome this limitation and predicts the bubble velocities better at the instants of bubble-wall collision. For the vertical bubble velocity, the CNN-based models tend to slightly underestimate, compared to other methods when the bubble deformation is the largest (e.g., at $t = 0.03$ and 0.18 in Fig. 6(b)). At this time, the bubble aspect ratio increases rapidly, i.e., the bubble shape shrinks abruptly along the rising (vertical)

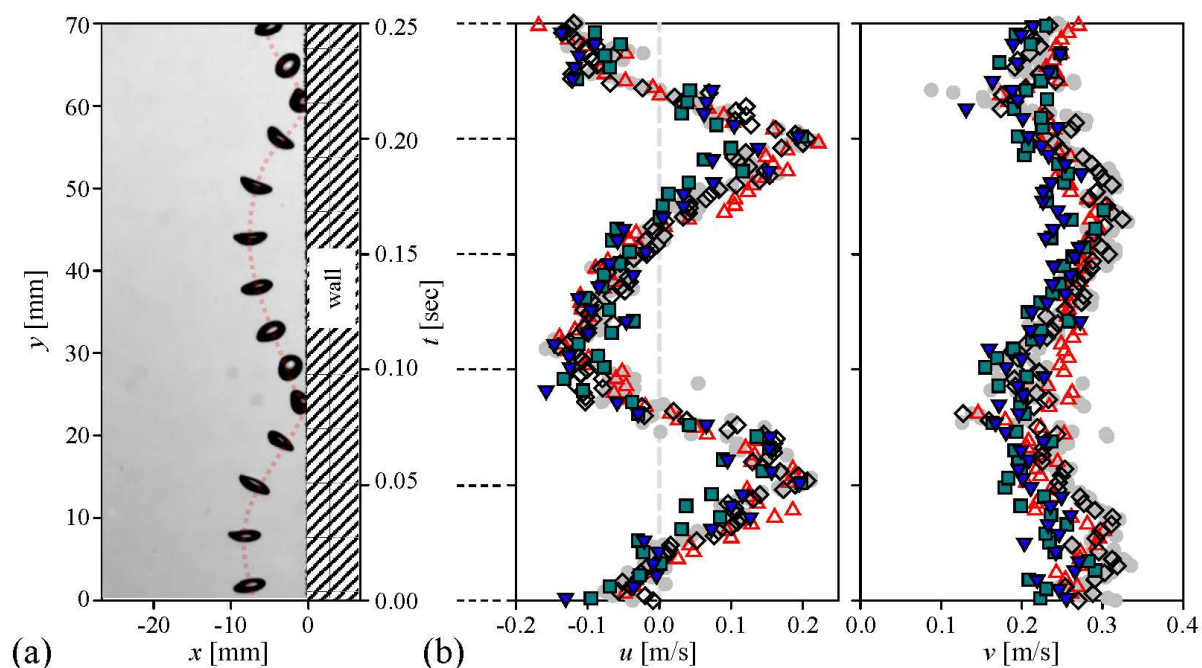


Fig. 6. Evaluation of the velocity of a single bubble rising (with bouncing) near the wall: (a) sequential bubble shadow images with the time interval of 20 msec. The dotted line denotes the bubble trajectory. (b) Corresponding time history of the horizontal (u) and vertical (v)

bubble velocities: ●, PTV; △, Lukas-Kanade method; ◇, Farnebäck method; ■, pre-trained CNN-based model; ▼, fine-tuned CNN-based model.

direction, by which the larger drag force acts on the bubble decelerating its movement. As noted, each method tested in the present study has a different dependency (or sensitivity) on the local bubble deformation (Fig. 5), and the traditional PTV cannot reflect the localized interfacial movement. It is noted that the relatively larger scatter in the data obtained by the CNN-based algorithms is attributed to the enhanced sensitivity to the bubble deformation.

Dilute bubble plume (void fraction < 10%)

Fig. 7 shows the time-averaged and root-mean-squared (r.m.s.) fluctuating velocities for the case of the dilute bubble plume (void fraction of 1.13%). The representative bubble shadow images evaluated are shown in Fig. 7(a), and the velocity profiles are obtained by averaging along the vertical (y) direction, as well. The time-averaged horizontal and vertical velocities were around 0 and around 0.3 m/s, which agrees with the previous result of the bubble plume with a similar condition (void fraction of 0.5-10%) (Riboux *et al.*^[1]). The conventional optical flow methods and fine-tuned CNN-based model provided quite accurate time-averaged velocities in both directions, compared to the PTV (Figs. 7(b) and (c)). However, unlike the case of a single bubble velocimetry, the mean bubble velocities estimated by the pre-trained PWC-Net tend to deviate a lot; in particular, the horizontal velocity did not represent the

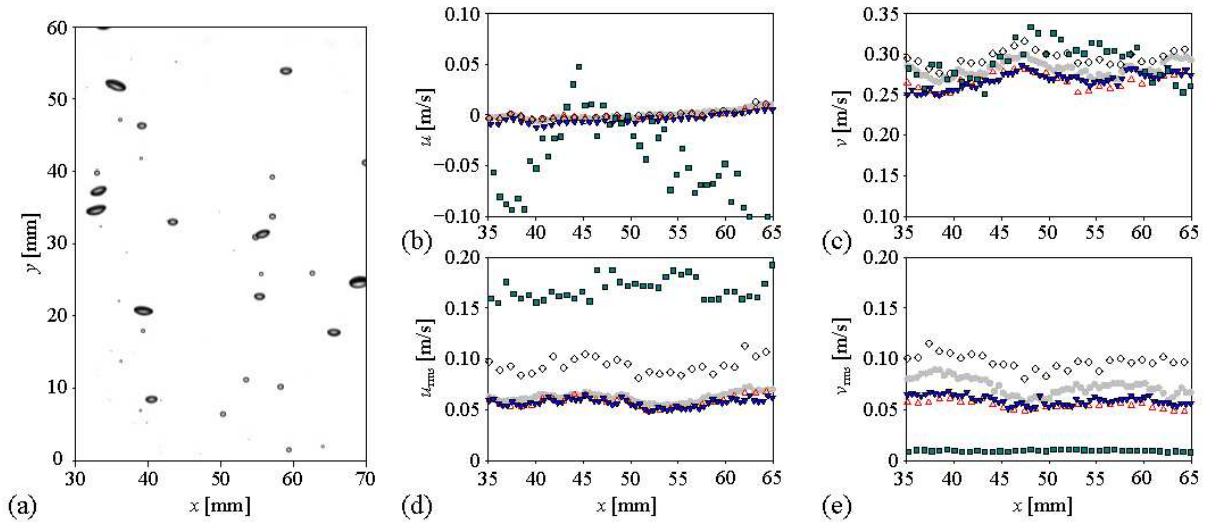


Fig. 7. Evaluation of the bubble velocity in the dilute bubble plume (1.13% void fraction): (a) instantaneous image of the dilute bubble plume; (b) horizontal velocity; (c) vertical velocity; (d) horizontal root-mean-square (r.m.s.) velocity; (e) vertical r.m.s. velocity. All velocity components were averaged in time and y -direction.

●, PTV; △, Lukas-Kanade; ◇, Farnebäck; ■, pre-trained CNN-based model; ▼, fine-tuned CNN-based model.

Farnebäck; ■, pre-trained CNN-based model; ▼, fine-tuned CNN-based model.

statistically symmetric nature of the uniform bubbly plume. This discrepancy clearly implies the importance of choosing the proper set of data to train the deep learning model. The pre-trained model (in this case, the original model was trained by the KITTI, SINTEL, and flyingchair dataset (Sun *et al.*^[35]) is optimized for calculating the velocities under the limited conditions (e.g., small void fraction of $< 0.2\%$) since it was trained with the image of objects with number of less than 10. In contrast, the re-trained PWC-Net was shown to measure the velocities of moving multi-objects ($\sim \mathcal{O}(10^2)$), as seen in Figs. 7(b) and (c). In terms of the vertical velocity (v), compared to the PTV data, the maximum deviation of the Lucas-Kanade, Farnebäck, pre-trained PWC-Net, and fine-tuned PWC-Net were 9.5, 8.8, 16.8, and 12.4%, and the average errors were 5.4, 4.6, 6.9 and 4.7%, respectively. Thus, it can be said that all the models except for the pre-trained CNN-based one showed a reasonable accuracy for the estimation of the first-order statistics of the bubble velocity.

In terms of the r.m.s. vertical and horizontal velocity fluctuation (Figs. 7(d) and (e)), interestingly, the performance of tested models is quite different. Following the mean vertical velocity, the pre-trained PWC-Net showed the most unreliable prediction, i.e., over- and under-estimation of the horizontal and vertical velocity fluctuations, respectively. It was found that the Lucas-Kanade method and the fine-tuned PWC-Net measure the r.m.s. velocity fluctuation quite accurately; the horizontal component agrees with the result of PTV while the vertical velocity fluctuation is slightly lower. This is related to the nature of the optical flows to capture the interfacial velocity, not the velocity of the bubble centroid, as we have discussed in Fig. 6(b). With the Farnebäck method, the r.m.s. fluctuation velocities in both directions were estimated to be quite higher compared to the PTV, which is attributed to the wide spatial variation in the calculated velocity, indicating that the assumption of the higher-order distribution of intensity would be over-specified and degrade the bubble velocity measurement. Similarly, the Lukas-Kanade method recognizes the image intensity as a smoothed image, resulting in the underestimation of r.m.s. fluctuation velocity (Fig. 7(e)). However, the CNN-based models are free from these assumptions and provide the results closest to the PTV.

Dense bubble plume (void fraction $> 10\%$)

Encouraged by the performance of optical flow algorithms as a bubble velocimetry, we applied the methods to the highly dense bubble plume with the void fraction of 58% (Fig. 2(c)), for which the conventional PTV-based approach is expected to suffer from the highly overlapped bubbles. Thus, the evaluation on the accuracy based on the comparison with the PTV would not be valid, and we will focus on examining how the measured bubble velocity using the optical flows are physically acceptable. The velocity fields (and the corresponding contour of horizontal bubble velocity) obtained by applying each method to the instantaneous flow (Fig. 8(a)) are shown in Figs. 8(b)-(f). With the PTV (Fig. 8(a)), the highly entangled bubbles make it almost impossible to identify the individual bubbles and they are recognized as one big object (represented by the large rectangular contours, of which the shape and size change inconsistently), and the non-physical velocity vectors (indicated by the arrows in Fig. 8(b)) directing the opposite direction to the bubble movement are obtained. On the other hand,

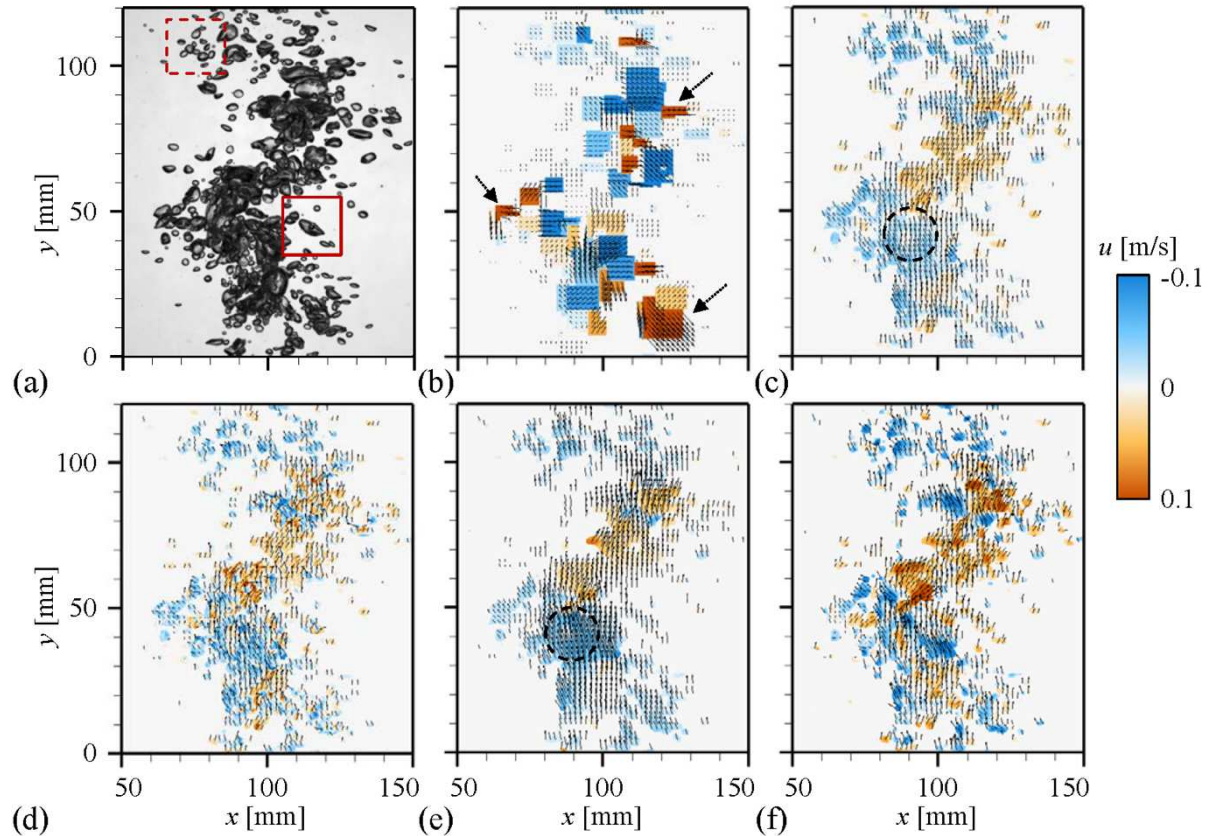


Fig. 8. Evaluation of the bubble velocity distribution in the dense bubble plume (58.1% void fraction): (a) raw image; (b) PTV; (c) Lukas-Kanade; (d) Farnebäck; (e) pre-trained CNN-based model; (f) fine-tuned CNN-based model. In (b)-(f), the color contour denotes the magnitude of the horizontal bubble velocity.

the optical flows are capable of revealing the unsteady kinematics and dynamics of the bubble plume as well as the bubble velocity distribution (Figs. 8(c)-(f)). Actually, to the best of our knowledge, this kind of quantitative characterization of the bubble velocities in the bubbly flow at the void fraction as high as 50% was not attempted and successful so far. Comparing the results among optical flow models, the details of the spatial variation in the measured velocity fields are found to be different. For the Lucas-Kanade method (Fig. 8(c)) and pre-trained PWC-Net (Fig. 8(e)), the spatial distribution of velocity is smoothed out (for example, see the area noted with dashed circle in the figure) at the positions with many overlapped interfaces (Fig. 8(a)). This is, respectively, attributed to the low-order assumption applied to the image intensity and the lack of relevant training with the multibody-velocity data, which were compensated by the Farneback and fine-tuned PWC-Net, respectively. As shown in Figs. 8(d) and (f), their results are relatively successful in detecting the sharp interfacial variations.

To examine this in detail, the bubble velocity distribution in the areas marked with dashed and solid boxes in Fig. 8(a) are shown in Figs. 9(b)-(f) and (h)-(l), respectively. The tested instantaneous images are again shown in Fig. 9(a) and (g), respectively, which show that the individual bubbles in the bubble cloud move in different directions to each other (see the supplementary movies 1 and 2, respectively). With the PTV (Figs. 9(b) and (h)), the overlapped bubbles are again recognized as a large area with the same horizontal velocity, failing to represent the actual bubble movements. The Lucas-Kanade (Figs. 9(c) and (i)) and pre-trained PWC-Net (Figs. 9(e) and (k)) produce the velocity vectors on each bubble to be directed along the same orientation, i.e., smoothed out artificially, and the horizontal movements of each

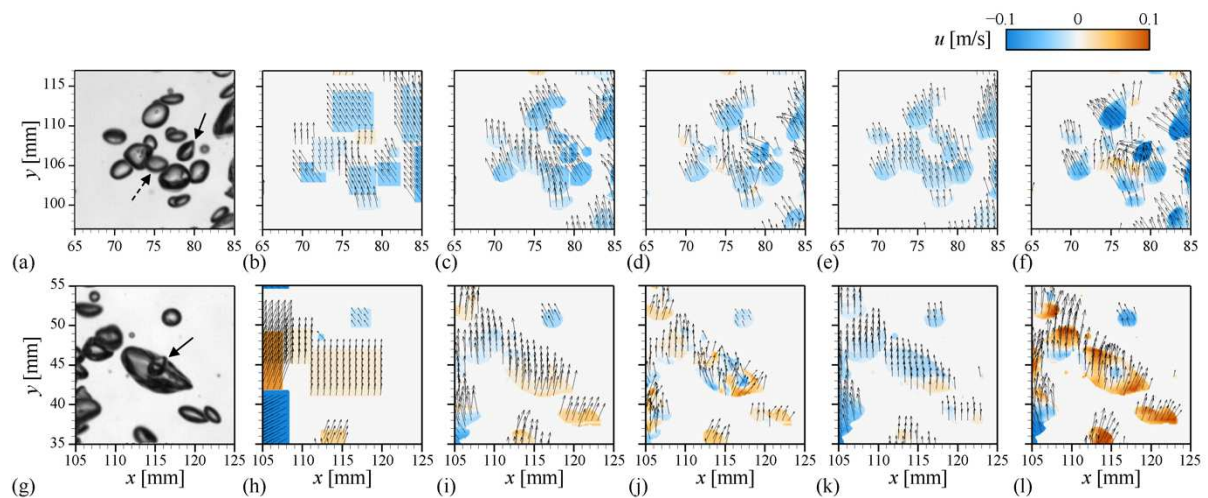


Fig. 9. Instantaneous velocity field with the horizontal velocity contour for the local areas highlighted in Fig. 8(a): (a, g) raw image; (b, h) PTV; (c, i) Lukas-Kanade; (d, j) Farneback; (e, k) pre-trained CNN-based model; (f, l) fine-tuned CNN-based model.

bubble observed in [supplementary movies 1 and 2](#) cannot be captured. On the contrary, the Farneback method ([Figs. 9\(d\) and \(j\)](#)) and fine-tuned PWC-Net ([Figs. 9\(f\) and \(l\)](#)) are capable of faithfully tracking and quantifying the movements of each bubble independently. Surprisingly, it is found that they can measure the velocity of the small bubble partially or fully covered by the larger ones ([Figs. 9\(j\) and \(l\)](#)), which is quite promising to consider that the conventional particle image velocimetry (PIV) is limited in evaluating the velocities across a wide scale range simultaneously^[37, 38] and the similar issue was raised in the recent deep-learning based bubble detection^[7]. For example, the bubble indicated by the dashed arrow in [Fig. 9\(a\)](#) solely translates to the right direction, while the surrounding bubbles are moving left (see the [supplementary movie 1](#)). This movement can be detected by the Farneback method ([Fig. 9\(d\)](#)) and fine-tuned PWC-Net ([Fig. 9\(f\)](#)), evidenced by the contour of horizontal velocity. As another example, the smaller bubble noted by a solid arrow in [Fig. 9\(g\)](#) is located inside the larger one and they have opposite horizontal velocities (see the [supplementary movie 2](#)). For this case, only the re-trained CNN-based model can accurately identify the velocity of the small bubble ([Fig. 9\(l\)](#)), while others produced unrealistic results. Thus, it is understood that the well-trained CNN-based optical flow, which is independent of any assumptions on the image intensity and the size effect of interrogation window, is the most robust and reliable on the interfacial complexity of bubbly flow.

Finally, the quantitative comparison of the velocity statistics obtained by each approach is provided in [Fig. 10](#). First, it is found that the time-averaged horizontal ([Fig. 10\(a\)](#)) and vertical ([Fig. 10\(b\)](#)) velocity components in general show the symmetric distribution with respect to the plume center at $x \sim 110$ mm. The mean horizontal velocity represents the well-known diverging tendency of the bubble plume, which is negative (positive) at the left (right) side of the plume. It is noted that the pre-trained PWC-Net measures the horizontal velocity that is biased to the negative value, indicating the limitation in the multi-body identification. On the other hand, the fine-tuned CNN model is capable of capturing the stiff gradient (change) of the horizontal velocity across the center, another well-known feature of the bubble plume^[40], compared to other methods. From all the methods, the profiles of mean vertical velocity follow the bell shape, typically reported in the literature^[22]. The results from the Farneback method and the fine-tuned PWC-Net are similar to each other, whereas the pre-trained PWC-Net slightly underestimates the velocity. For the root-mean-squared velocity fluctuation ([Figs. 10\(c\) and \(d\)](#)), the results of the Farneback method and fine-tuned PWC-Net are higher than the others in both directions, since they are capable of reflecting the localized flow variations while

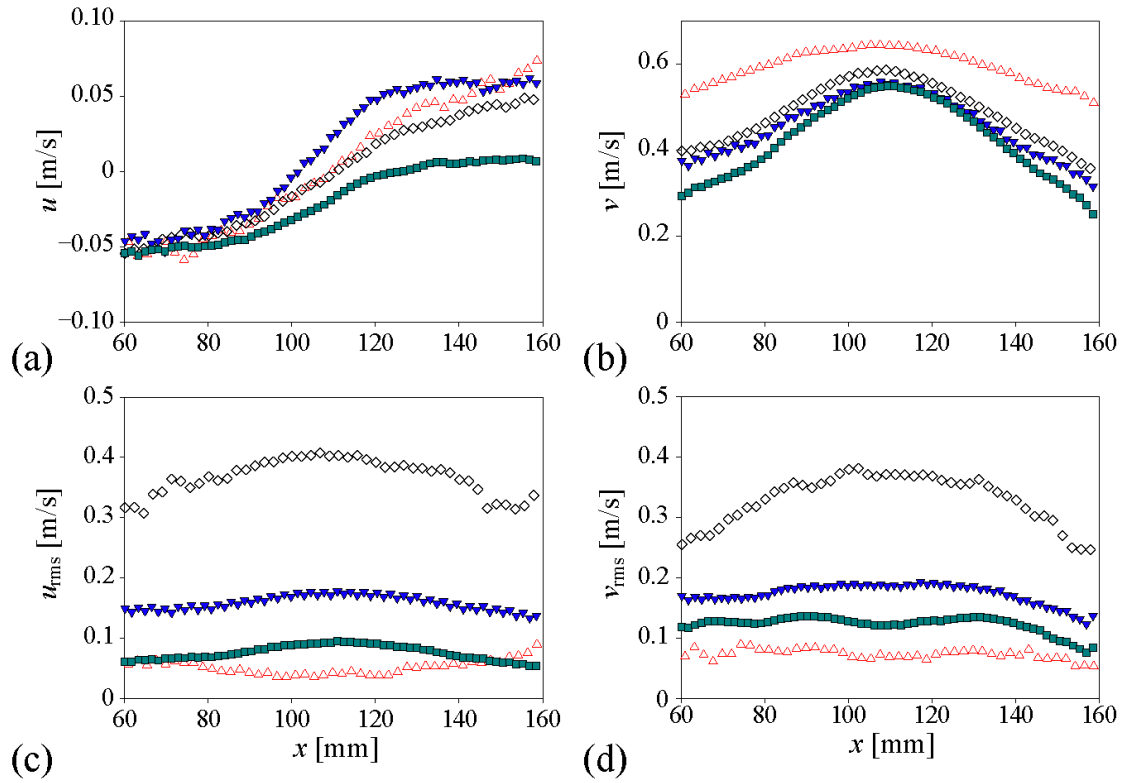


Fig. 10. Bubble velocity profiles in the dense bubble plume: (a) time-averaged horizontal velocity; (b) time-averaged vertical velocity; (c) horizontal r.m.s. velocity fluctuation; (d) vertical r.m.s. velocity fluctuation. \triangle , Lukas-Kanade; \diamond , Farneback; \blacksquare , pre-trained CNN-based model; \blacktriangledown , fine-tuned CNN-based model. All velocities were averaged along the vertical (y) direction in the measurement plane.

the others make the velocity field smoothed, as discussed above. Interestingly, depending on the methods, the r.m.s. velocity fluctuation is distributed in different manners; for example, the vertical component follows the concave (Lucas-Kanade method) or convex (others) profile (Fig. 10(c)). Currently, it is not clearly understood how this change is incurred and it would an interesting topic to investigate as a future work.

CONCLUDING REMARKS

In the present study, we have successfully demonstrated that the optical flow algorithms can be utilized as a new bubble velocimetry in experimentally investigating the gas-liquid two-phase flows in a very complex environment, such as the high volume void fraction. As candidates for the potential algorithm, the conventional methods of Lucas-Kanade and Farneback model and CNN-based models of pre-trained and fine-tuned PWC-Net were tested

using the high-speed bubble shadowgraph images obtained for three different configurations (single bubble rising near the solid wall, dilute bubble plume, and dense bubble plume). To optimize the optical flows, the effect of the interrogation window size (for the conventional optical flow) and the fine-tuning with the synthetic bubble images (for the CNN-based model) were systematically performed. Compared with the result of the PTV, it is found that the proposed optical flows, in general, correctly measure the temporal variation of the bubble velocity, in particular when there is only one bubble in the image. However, as the bubble number density increases substantially, which is our major motivation to develop new bubble velocimetry, the optical flow algorithms performed differently depending on their assumptions and level of training. For example, the CNN-based model that was not properly trained with the bubbly flow data did not perform well to capture the locally varying nature of bubble interface even in the case of dilute bubble plume, in which multiple bubbles simultaneously rise but rarely overlap. However, the re-trained CNN-based model (PWC-Net) was shown to be fully applicable even to the dense bubble plume, for which the traditional PTV approaches cannot produce any physically meaningful data. In overall, the Farnebäck and fine-tuned (re-trained) PWC-Net models tend to faithfully reflect the detailed spatial variation of each bubble velocity, being rigorously checked by comparing with the bubble motion from the raw image. Considering the accuracy of statistically higher-order flow variations and lower computational cost, on the other hand, it is concluded that the fine-tuned PWC-Net is recommended over the Farnebäck method as a new bubble velocimetry (see the [supplementary move 3](#)).

We have shown that the intensity-based (optical) algorithm can be very useful as an accurate measurement tool of bubble velocity, and hopefully replaced the traditional method (e.g., PTV), which uses the identification-based principle. To guarantee better accuracy and applicability, the relation between the interfacial deformation and the calculated velocity field inside the bubble should be understood physically, which may require detailed information and mechanism involved in bubble deformation (wobbling). Also, the change in the architecture of the CNN-based model should affect the performance significantly, which will be an interesting topic for future work. Finally, we believe that the optimized CNN-model in the present study will also perform well for the other bubbly flows, since it was shown to successfully evaluate the two-phase flow (dense bubble plume) although it was not trained with the same data set. The optimized bubble velocimetry algorithm is available online (<https://github.com/dae416/DeepBubbleVelocimetry>), and we hope it can accelerate the further experimental investigations of the gas-liquid two-phase flows of a higher void fraction in a

complex geometry.

METHODS

The apparatus for bubbly flows and shadowgraphy

To establish the bubbly flows, the rectangular reservoir with the size of $1000 \times 1000 \times 1000$ mm³ is filled with tap water and the air is injected through the sparger placed at the bottom of the reservoir, which is pressurized by the 4-HP air compressor (Airbank; AB350). The flow rate of air is controlled by the pressure regulator, through which the three different void fractions (α) are achieved: ~ 0 (single rising bubble), 1.13% (dilute bubble plume), and 58% (dense bubble plume) (Figs. 2(a)-(c)). With increasing α from 1.13% to 58%, the size distribution of bubble, which follows the typical log-normal curve^[22], broadens from 2.1-4.9 mm (where the median diameter, d_{50} , is 3.25 mm) to 1.6-5.4 mm ($d_{50} = 3.47$ mm). For the dimensionless parameter, the Reynolds and Weber number, defined as $Re = \rho_l d_{50} v_{avg} \mu_l^{-1}$ and $We = \rho_l v_{avg}^2 d_{50} \sigma_l^{-1}$ respectively, ranges as 750-1,910 and 2.4-15.0. To capture the bubble image, the light source and the diffusion plate is placed at one side of the reservoir, and the high-speed camera (Speedsense M310; Dantec Dynamics) is located at the opposite side, of which the spatial resolution is 1920×1080 pixels and the sampling rate is 1000 Hz (sufficient to capture the unsteady bubble shape and motion). Based on the convergence test, we have found that the bubble statistics are converged when they are averaged over 200 pairs of bubble images, which were adopted in this study to validate the measured bubble velocities.

Conventional particle tracking velocimetry (PTV)

The PTV is performed using the in-house code, which consists of the binarization, identification, and evaluation, as shown in Figs. 1(a)-(d). First, the shadow image of bubbles (or the bubble plume) is binarized using the Sauvola adaptive algorithm^[7]. Then, the bright area inside the bubble is filled to avoid underestimating the bubble size. Next, the out-focused bubbles are excluded by thresholding the lower magnitude of intensity gradient at the bubble edge, and the overlapped bubbles are separated with the watershed transform^[5]. For each time interval, the center locations of identified bubbles are collected. To evaluate the velocity vector, the bubble centers at two consecutive time instants are matched with the assumption that they

are closest than others, while the outlier vectors are eliminated when the vector magnitude exceeds the prescribed threshold. Finally, the distance between location pairs is calculated and divided by the time interval between consecutive images, resulting in the bubble velocities (Fig. 1(d)). The procedure of the PTV is performed by CPU (Intel® Core™ i7-5960X CPU @3.00GHz), and the time costs for each sub-process are outlined in Table 1.

References

1. G. Riboux, F. Risso, and D. Legendre, “Experimental characterization of the agitation generated by bubbles rising at high Reynolds number,” *J. Fluid Mech.* **643**, 509-539 (2010).
2. E. Bouche, V. Roig, F. Risso, and A. M. Billet, “Homogeneous swarm of high-Reynolds-number bubbles rising within a thin gap. Part 1. Bubble dynamics,” *J. Fluid Mech.* **704**, 211-231 (2012).
3. M. Kim, J. H. Lee, and H. Park, “Study of bubble-induced turbulence in upward laminar bubbly pipe flows measured with a two-phase particle image velocimetry,” *Exp. Fluids* **57**, 55 (2016).
4. H. Hessenkemper and T. Ziegenhein, “Particle Shadow Velocimetry (PSV) in bubbly flows,” *Int. J. Multiph. Flow* **106**, 268-279 (2018).
5. J. Lee and H. Park, “Bubble dynamics and bubble-induced agitation in the homogeneous bubble-swarm past a circular cylinder at small to moderate void fractions,” *Phys. Rev. Fluids* **5**, 54304 (2020).
6. B. Hohermuth, M. Kramer, S. Felder, and D. Valero, “Velocity bias in intrusive gas-liquid flow measurements,” *Nat. Commun.* **12**, 4123 (2021).
7. Y. Kim and H. Park, “Deep learning-based automated and universal bubble detection and mask extraction in complex two-phase flows,” *Sci. Reports* **11**, 1-11 (2021).
8. J. H. Lee, H. Kim, J. Lee, and H. Park, “Scale-wise analysis of upward turbulent bubbly flows: An experimental study,” *Phys. Fluids* **33**, 053316 (2021).
9. H. Kim and H. Park, “Bubble dynamics and induced flow in a subcooled nucleate pool boiling with varying subcooled temperature,” *Int. J. Heat Mass Transf.* **183**, 122054 (2022).
10. J. Lee and H. Park, “Flow induced by a single-bubble chain depending on the bubble release frequency,” *Phys. Fluids* **34**, 033312 (2022).
11. P. G. Saffman, “On the rise of small air bubbles in water,” *J. Fluid Mech.* **1**, 249-275 (1956).
12. T. J. Chuang & T. Hibiki, “Interfacial forces used in two-phase flow numerical simulation,”

- Int. J. Heat Mass Transf. 113, 741-754 (2017).
13. I. Khan, M. Wang, Y. Zhang, W. Tian, G. Su, and S. Qiu, "Two-phase bubbly flow simulation using CFD method: A review of models for interfacial forces," *Prog. Nucl. Energy* 125, 103360 (2020).
 14. M. Lance and J. Bataille, "Turbulence in the liquid phase of a uniform bubbly air-water flow," *J. Fluid Mech.* **222**, 95-118 (1991).
 15. R. F. Mudde, "Gravity-Driven Bubbly Flows," *Annu. Rev. Fluid Mech.* **37**, 393-423 (2005).
 16. J. Rensen, S. Luther, and D. Lohse, "The effect of bubbles on developed turbulence," *J. Fluid Mech.* **538**, 153-187 (2005).
 17. S. Hosokawa and A. Tomiyama, "Bubble-induced pseudo turbulence in laminar pipe flows," *Int. J. Heat Fluid Flow* **40**, 97-105 (2013).
 18. F. Risso, "Agitation, mixing, and transfers induced by bubbles," *Annu. Rev. Fluid Mech.* **50**, 25-48 (2018).
 19. E. Alméras, O. Masbernat, F. Risso, and R. O. Fox, "Fluctuations in inertial dense homogeneous suspensions," *Phys. Rev. Fluids* **4**, 102301 (2019).
 20. D. Legendre, R. Zenit, and J. R. Velez-Cordero, "On the deformation of gas bubbles in liquids," *Phys. Fluids* **24**, 043303 (2012).
 21. D. P. M. Van Gils, D. Narezo Guzman, C. Sun, and D. Lohse, "The importance of bubble deformability for strong drag reduction in bubbly turbulent Taylor-Couette flow," *J. Fluid Mech.* **722**, 317-347 (2013).
 22. C. C. K. Lai and S. A. Socolofsky, "The turbulent kinetic energy budget in a bubble plume," *J. Fluid Mech.* **865**, 993-1041 (2019).
 23. A. U. M. Masuk, A. K. R. Salibindla, and R. Ni, "The orientational dynamics of deformable finite-sized bubbles in turbulence," *J. Fluid Mech.* **915**, 1-17 (2021).
 24. S. Perrard, A. Rivière, W. Mostert, and L. Deike, "Bubble deformation by a turbulent flow," *J. Fluid Mech.* **920**, 1-27 (2021).
 25. S. A. Socolofsky, E. E. Adams, and C. R. Sherwood, "Formation dynamics of subsurface hydrocarbon intrusions following the Deepwater Horizon blowout," *Geophys. Res. Lett.* **38**, L09602 (2011).
 26. A. Bombač, Z. Rek, and J. Levec, "Void fraction distribution in a bisectonal bubble column reactor," *AIChE J.* **65**, 1186-1197 (2019).
 27. M. C. Boufadel, S. Socolofsky, J. Katz, D. Yang, C. Daskiran, and W. Dewar, "A Review on Multiphase Underwater Jets and Plumes: Droplets, Hydrodynamics, and Chemistry," *Rev.*

- Geophys. **58**, e2020RG000703 (2020).
28. J. B. Roerdink, and A. Meijster, “The watershed transform: Definitions, algorithms and parallelization strategies,” *Fundam. Inform.* **41**, 187-228. (2000).
 29. T. Liu and L. Shen, “Fluid flow and optical flow,” *J. Fluid Mech.* **614**, 253-291 (2008).
 30. S. Cai, E. Mémin, P. Dérian, and C. Xu, “Motion estimation under location uncertainty for turbulent fluid flows,” *Exp. Fluids* **59**, 149-176 (2018).
 31. S. Anthwal and D. Ganotra, “An overview of optical flow-based approaches for motion segmentation,” *Imaging Sci. J.* **67**, 284-294 (2019).
 32. B. D. Lucas and T. Kanade, “An Iterative Image Registration Technique with an Application to Stereo Vision,” *Proc. Seventh Int’l Joint Conf. Artificial Intelligence*, vol. 81, 674-679 (1981).
 33. G. Farneäck, “Two-frame motion estimation based on polynomial expansion,” *Proc. Scandinavian Conf. Image Anal.*, 363-370 (2003).
 34. A. Dosovitskiy, P. Fischer, E. Ilg, P. Hausser, C. Hazirbas, V. Golkov, and T. Brox, “FlowNet: Learning optical flow with convolutional networks,” *IEEE I. Conf. Comp. Vis.*, 2758-2766 (2015).
 35. D. Sun, X. Yang, M. Y. Liu, & J. Kautz, “PWC-Net: CNNs for optical flow using pyramid, warping, and cost volume,” *In Proceedings of the IEEE conference on computer vision and pattern recognition*, 8934-8943 (2018).
 36. Y. Lee, H. Yang, & Z. Yin, “PIV-DCNN: cascaded deep convolutional neural networks for particle image velocimetry,” *Exp. Fluids*, **58**, 1-10 (2017).
 37. S. Cai, S. Zhou, C. Xu, & Q. Gao, “Dense motion estimation of particle images via a convolutional neural network,” *Exp. Fluids*, **60**, 1-16 (2019).
 38. F. Scarano, “Iterative image deformation methods in PIV,” *Meas. Sci. Technol.*, **13**, R1 (2001).
 39. L. P. N. Mendes, A. M. C. Ricardo & A. J. M. Bernardino, “A comparative study of optical flow methods for fluid mechanics,” *Exp Fluids* **63**, 7 (2022).
 40. D. Yang, B. Chen, S. A. Socolofsky, M. Chamecki, & C. Meneveau, “Large-eddy simulation and parameterization of buoyant plume dynamics in stratified flow,” *J. Fluid Mech.*, **794**, 798-833 (2016).

Acknowledgment

This work was supported by grants (2020R1A2C2014510, 2021R1A4A1032023) through

the National Research Foundation of Korea (NRF) funded by the Korean government (MSIT), research project (20210584) funded by the Korea Coast Guard, Korea, and Institute of Engineering Research at Seoul National University.

Author Contributions

D.C., H.K., and H.P. developed the problem and designed the research project. D.C. and H. K. conducted the optimization of the training and evaluation of the algorithm. H.P. supervised the project. D.C., H.K., and H.P. contributed to the writing and development of the manuscript.

Competing Interests

The authors declare no competing financial interests.

Supplementary Information

There are supplementary movies accompanied.

Data availability

All data generated or analyzed during this study are included in this published article and supplementary information files.

Supplementary Files

This is a list of supplementary files associated with this preprint. Click to download.

- [supplementarymovie1.mp4](#)
- [supplementarymovie2.mp4](#)
- [supplementarymovie3.mp4](#)